RSC Advances

ROYAL SOCIETY OF CHEMISTRY

www.rsc.org/advances

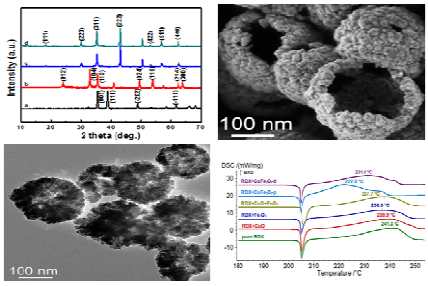

Hollow $CuFe_2O_4$ nanospheres show high catalytic activity on the thermal decomposition of RDX and FOX-7.

Catalytic decomposition action of hollow $CuFe_2O_4$ nanospheres on RDX and FOX-7

Yu Zhang[a,b], Taotao Wei[a], Kangzhen Xu[a,*], Zhaoyu Ren[a,*],

Libai Xiao[c], Jirong Song[a], Fengqi Zhao[c]

[a] *School of Chemical Engineering, Institute of Photonics & Photon-Technology, Northwest University, Xi'an 710069, PR China*

[b] *College of Chemistry and Chemical Engineering, Xinyang normal University, Xinyang, 464000, PR China*

[c] *Xi'an Modern Chemistry Research Institute, Xi'an 710065, PR China*

Abstract: Two hollow $CuFe_2O_4$ nanospheres ($CuFe_2O_4$-p and $CuFe_2O_4$-d) were successfully prepared using a hydrothermal method. $CuFe_2O_4$-p has samller size and higher BET specific surface area compared to $CuFe_2O_4$-d. The catalytic activity of nano-CuO, nano-Fe_2O_3, physically mixed CuO+Fe_2O_3, $CuFe_2O_4$-p, and $CuFe_2O_4$-d on the thermal decomposition of RDX and FOX-7 were comparatively investigated by differential scanning calorimetry (DSC) method. The results showed that $CuFe_2O_4$-p and $CuFe_2O_4$-d exhibited higher catalytic activity than the others, and the apparent activation energies of decomposition were reduced by 37.7 and 28.4 kJ mol^{-1} for RDX, 40.1 and 30.5 kJ mol^{-1} for FOX-7, respectively. The catalytic performance of $CuFe_2O_4$-p for the decompositions of RDX and FOX-7 was superior to that of $CuFe_2O_4$-d.

Keywords: $CuFe_2O_4$, Catalytic action, RDX, FOX-7, Thermal decomposition

1. Introduction

Cyclotrimethylenetrinitramine (RDX) and 1,1-diamino-2,2-dinitroethylene (FOX-7), known as two common oxidizers, play key roles in composite solid propellants. Their thermal decomposition characteristics directly influence the combustion behavior of solid propellant: the lower thermal decomposition temperature and apparent activation energy, the shorter ignition delay time and the higher burning rate of propellant [1,2]. It is widely acknowledged that catalysts can accelerate the oxidizer decomposition and enhance the burning rate of propellant [3-6].

* Corresponding author.
E-mail address: xukz@nwu.edu.cn, rzy@nwu.edu.cn

Nano metal oxides exhibit high catalytic activity because of their large surface area, the high mobility of their surface atoms, and varied lattice defects [7-11]. In the past decades, the thermal decompositions of RDX and FOX-7 have been extensively investigated by taking advantage of the catalytic activities of a single metal oxide and two physically mixed components. The most commonly used catalysts are transition metal oxides, such as Fe_2O_3 [12,13], CuO [14,15], MnO_2 [16], and V_2O_3 [17]. As previously demonstrated, binary mixed metal oxides have better catalytic effect than a single one, because the performance of two kinds of metal oxides would be complementary and have a "synergistic effect" [18-21].

Nano metal composite oxides possess specific structure-properties and higher chemical stability (acid and alkali resistance), and two types of metals can generate a "synergistic effect" [22,23]. Therefore, they have been extensively studied in recent years and used in many high and new fields, such as photoelectric materials, magnetic materials and photocatalysis [24-26]. Among ferrites, $CuFe_2O_4$ has a cubic close-packed arrangement of oxygen ions with Cu^{2+} and Fe^{3+} ions at two different crystallographic sites [27, 28]. Owing to the unique electronic configuration of its valence shell (3d10 4s1), low price, environmental benignity, and the large abundance of Cu, $CuFe_2O_4$ has attracted extensive attention and is widely applied in sensors [29,30], batteries [31,32], and catalysts [33-35]. In our work, we attempt to use $CuFe_2O_4$ as burning catalysts in the special field of solid propellant, instead of single metal oxides and their physical mixtures.

In this paper, we report the preparation of two hollow $CuFe_2O_4$ nanospheres and explore its catalytic decomposition action on RDX and FOX-7 in compared with other related metal oxides.

2. Experimental

2.1 Preparation

Hollow $CuFe_2O_4$ spheres were synthesized using a hydrothermal method. We dissolved 4 mmol $CuCl_2{\cdot}2H_2O$, 8 mmol $FeCl_3{\cdot}6H_2O$, and 12 mmol NaAc in 70 mL ethylene glycol, following which we added 1.0 g polyvinylpyrrolidone (PVP)

(denoted as $CuFe_2O_4$-p) or dodecyl trimethyl ammonium bromide (DTAB) (denoted as $CuFe_2O_4$-d) as dispersants. The mixtures were stirred vigorously for 1 h, sealed in a 100 mL Teflon-lined stainless-steel autoclave, and heated at 180 ºC in air for 12 h. The resulting black solid products were collected through centrifugation and washed with ethanol and deionized water several times. All the generated samples were dried at 60 ºC. Finally, the $CuFe_2O_4$-p and $CuFe_2O_4$-d samples were prepared.

For comparison, nano-CuO, nano-Fe_2O_3 were prepared according to the methods in Ref. [12] and [14], respectively. Briefly, $CuCl_2 \cdot 2H_2O$ (15 mmol) were dissolved in 100 mL NaOH solution (3.2 M), 100 mL H_2O_2 (50 wt.%) was then added drop wise under constant stiring. The precipitate products were washed and dired at 110 ºC. After caclined at 350 ºC for 2 h, CuO sample was synthesized. For nano-Fe_2O_3, $FeCl_3 \cdot 6H_2O$ (4 mmol), urea (15 mmol), glycine (6.5 mmol), and 30 mL distilled water were added into a Teflon-lined stainless-steel autoclave (50 mL) with magnetic stirring, and then maintained at 160 ºC for 10 h. Subsequently, the products were washed and dried at 60 ºC. The resulting powder was used as the Fe_2O_3 sample. Besides, physically mixed CuO and Fe_2O_3 (1:1 mol/mol, denoted as CuO+Fe_2O_3) was obtained through mixing and grinding with CuO and Fe_2O_3 in the molar ratio of 1:1.

2.2 Equipments and Conditions

X-ray diffraction (XRD) patterns were acquired using a Rigarku Mini Flex 600 X-ray diffractometer with Cu Kα radiation. X-ray photoelectron spectroscopy (XPS) measurements were performed using a Thermo Scientific ESCALAB 250Xi X-ray photoelectron spectrometer. Scanning electron microscopy (SEM) images were recorded using a Zeiss SIGMA scanning electron microscope. Transmission electron microscopy (TEM) images and high-resolution TEM (HRTEM) images were obtained using an FEI Tecnai G2 microscope operated at 200 kV, and energy dispersive spectrum (EDS) mappings were acquired using an Oxford 51-XMX. N_2 adsorption-desorption isotherms at 77 K were measured using an Autosorb-iQ automated gas sorption system (Quantachrome Instrument). The specific surface area was calculated according to the Brunauere Emmette Teller (BET) method and the

pore volume was calculated based on the Barrett Joyner Halenda (BJH) equation.

The as-prepared CuO, Fe_2O_3, CuO+Fe_2O_3, $CuFe_2O_4$-p, and $CuFe_2O_4$-d were fully mixed with RDX and FOX-7 in the molar ratio of 1:4, and the mixtures were used as samples for DSC tests, which were performed using a 200F3 differential scanning calorimeter (Netzsch, Germany) with the following conditions: nitrogen gas purity, 99.999%; N_2 flow rate, 40 mL min^{-1}; sample mass, approximately 0.5 mg; heating rate (β), 5.0, 10.0, 15.0, and 20.0 °C min^{-1}.

3. Results and discussion

3.1 Characterization

Fig. 1 shows the XRD diffraction patterns of the as-prepared samples. The patterns of **Fig. 1a**,**b** could be indexed to CuO (JCPDS File No. 45-0937) and Fe_2O_3 (JCPDS File No. 33-0664), respectively. It can be seen from **Fig. 1c**,**d** that almost all the diffraction peaks can be well assigned to $CuFe_2O_4$ with a cubic spinel structure (JCPDS File No. 77-0010, space group: Fd-3m [227] with lattice parameters a = b = c = 8.37 Å). The diffraction peaks are at 2θ = 18.344º, 30.175º, 35.543º, 43.199º, 53.596º, 57.135º and 62.744º, which correspond to the crystal planes of (111), (220), (311), (400), (422), (511) and (440), respectively.

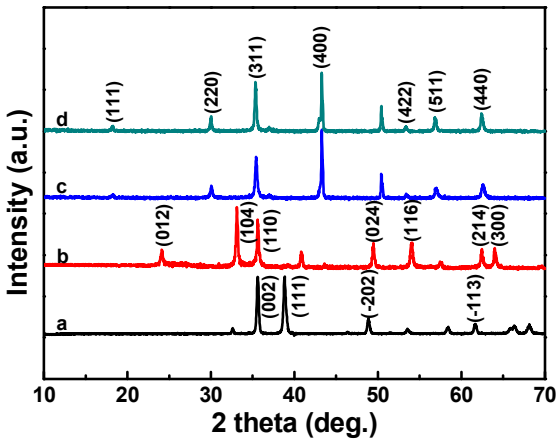

Fig. 1. XRD patterns of (a) CuO, (b) Fe_2O_3, (c) $CuFe_2O_4$-p and (d) $CuFe_2O_4$-d

The surface composition and chemical state of $CuFe_2O_4$ nanoparticle were further investigated by XPS. In the survey spectrum (**Fig. 2a**), the elements Cu, Fe and O can

be observed clearly. The appearance of C1s peaks was mainly due to the adsorbed or bonded organic species. The O 1s spectrum (**Fig. 2b**) can be deconvoluted into two peaks at 529.4 and 531.5 eV, which correspond to the O^{2-} ions and −OH groups, respectively. From **Fig. 2c**, the main peaks at 710.9 eV and the shoulder peak at 724.6 eV can be assigned to Fe $2p_{3/2}$ and Fe $2p_{1/2}$, respectively. The accompanying satellite peaks at around 718.2 eV were indicative of the presence of Fe^{3+} cations. No Fe^{2+} peak was observed. **Fig. 2d** shows the binding energies of Cu $2p_{3/2}$ and Cu $2p_{1/2}$ at 933.5 and 954.2 eV respectively, with a typical satellite peak of Cu^{3+} at 943.3 eV. These results further confirm that $CuFe_2O_4$ has been synthesized successfully.

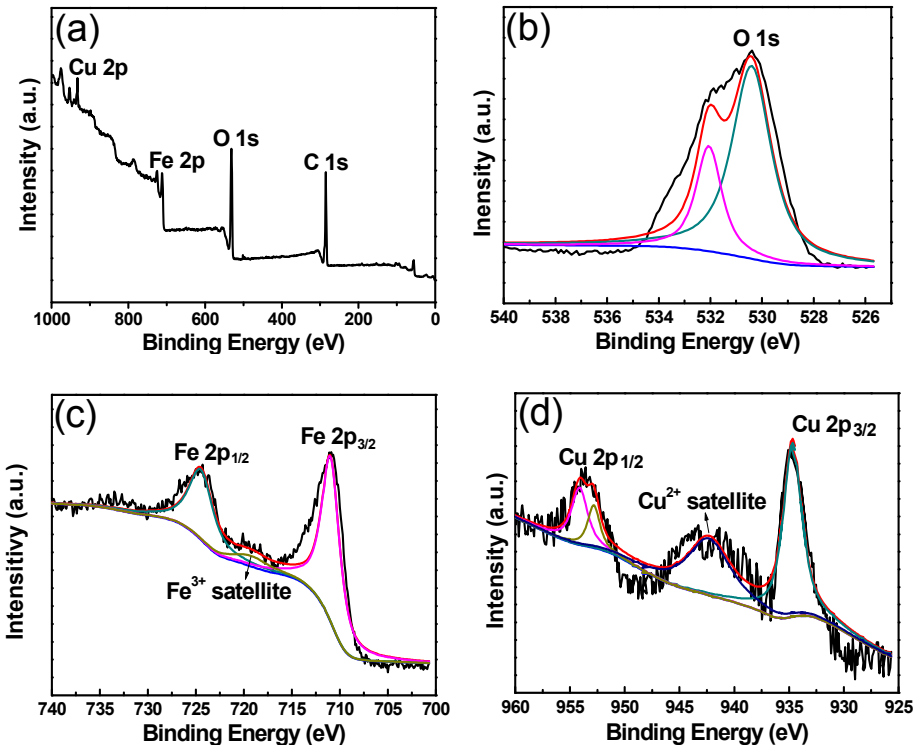

Fig. 2. XPS characterization of $CuFe_2O_4$, (a) survey spectra, (b) O 1s spectra, (c) Fe 2p spectra, and (d) Cu 2p spectra.

The morphology and structure of the as-prepared samples were characterized by SEM. It can be observed that the CuO sample consists of irregular bloks of sizes in the range of 400−500 nm (**Fig. 3a**). As shown in **Fig. 3b**, a large amount of Fe_2O_3 nanoparticles aggregate and form a well-defined spherical structure, the diameter of which is estimated as approximately 500 nm. Form **Fig. 3c**, we can obviously found

that Fe_2O_3 particles were dispersed on the surface of CuO samples. Owing to the limitation of physical blending, Fe_2O_3 and CuO were not well-mixed. **Fig. 3d,e** clearly show that $CuFe_2O_4$-p and $CuFe_2O_4$-d are composed of quasi-spherical particles with an average size of approximately 200 nm. The surfaces of the two $CuFe_2O_4$ spheres are rough, and the diameters are uniform. Obviously, the particle size of $CuFe_2O_4$-p is smaller than that of $CuFe_2O_4$-d. Thus, PVP is better than DTAB as the dispersant for the preparation of $CuFe_2O_4$ nanospheres. **Fig. 3f** displays the hollow structure of the $CuFe_2O_4$ nanosphere. The outer diameter of the hollow is approximately 200 nm and the inner diameter is about 150 nm on average. Such a hollow structure is very favourable to increase the specific surface areas and diffusion rate of reaction molecules.

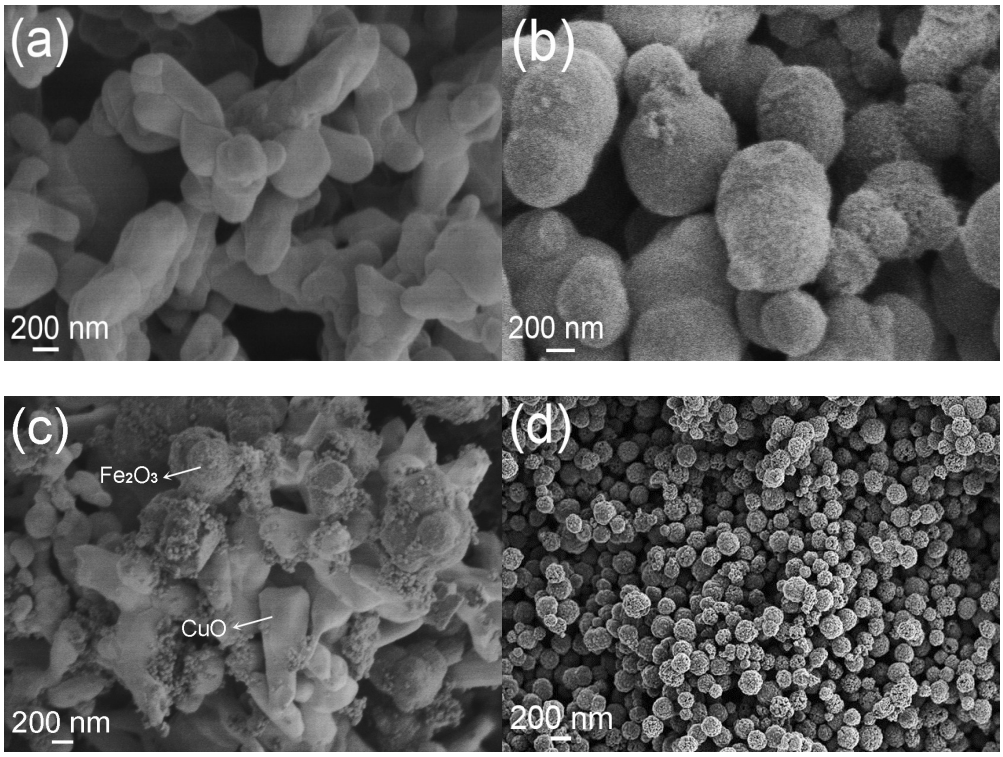

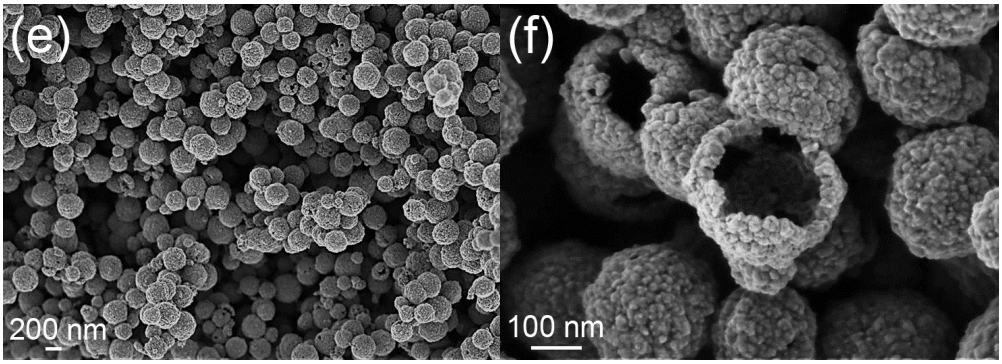

Fig. 3. SEM images of (a) CuO, (b) Fe_2O_3, (c) CuO+Fe_2O_3, (d) $CuFe_2O_4$-p, and (e,f) $CuFe_2O_4$-d.

The TEM images of $CuFe_2O_4$-p and $CuFe_2O_4$-d samples (**Fig. 4a,b**) further demonstrates their hollow nanospherical microstructure, which is consistent with the SEM results. In order to verify the crystalline structure of the $CuFe_2O_4$, we acquired the HRTEM image shown in **Fig. 4c**, which indicates that the $CuFe_2O_4$ nanoparticles show a well-defined lattice plane with a high degree of crystallinity. The lattice spacing of 0.248 nm corresponds to the (400) lattice planes and matches well with the value observed from the JCPDF file (No. 77-0010) of $CuFe_2O_4$. As shown in **Fig. 4d**, the corresponding selected-area electron diffraction (SAED) pattern indicates the polycrystalline feature of $CuFe_2O_4$ samples. EDS results (**Fig. 4e**) confirm the presence of Cu, Fe and O elements in $CuFe_2O_4$ nanoparticles. Atomic contents of Cu and Fe are 8.19% and 16.18% respectively, and the atomic ratio of the two elements is 1:1.98, which is close to theoretical molar ratio of $CuFe_2O_4$.

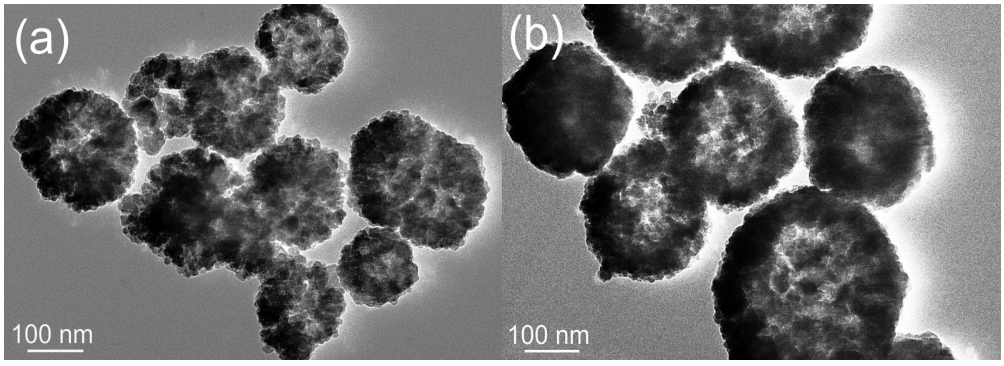

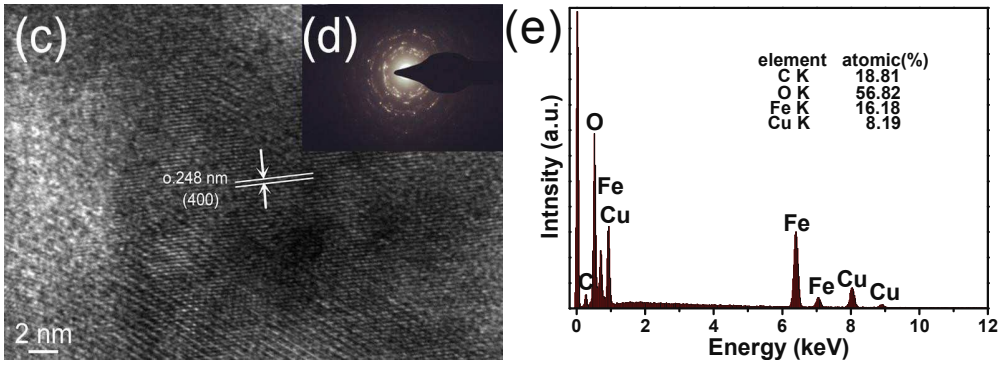

Fig. 4. TEM images of (a) $CuFe_2O_4$-p, (b) $CuFe_2O_4$-d;

HRTEM image of (c) $CuFe_2O_4$-p;

SAD pattern of (d) $CuFe_2O_4$-p; EDS analysis results of (e)$CuFe_2O_4$

To evaluate the specific surface areas and porosity of the as-prepared samples, N_2 adsorption-desorption isotherms were measured. The corresponding textural parameters are summarized in Table 1. The BET specific surface area of Fe_2O_3 is as large as that of $CuFe_2O_4$, whereas the surface areas of CuO and CuO+Fe_2O_3 are much lower than that of $CuFe_2O_4$. Note that the surface area of $CuFe_2O_4$-p (32.66 $m^2 g^{-1}$) is higher than that of $CuFe_2O_4$-d (28.97 $m^2 g^{-1}$). The larger specific surface area of the nanocomposite can offer more adsorpotion and reaction sites, leading to enhanced catalytic activity.

Table 1 Textural properties of as-prepared samples

Sample	S_{BET}[a] ($m^2 g^{-1}$)	V_{total}[b] ($cm^3 g^{-1}$)	D_{aver} (nm)
CuO	6.70	0.005	6.03
Fe_2O_3	32.07	0.094	11.77
CuO+Fe_2O_3	17.43	0.048	11.07
$CuFe_2O_4$-p	32.66	0.093	11.36
$CuFe_2O_4$-d	28.97	0.081	15.43

[a] Total surface area calculated using the BET method.

[b] Total pore volume calculated at $P/P_0 = 0.95$.

3.2 Influence on thermal decomposition of RDX

DSC results (**Fig. 5**) indicate that the peak temperatures of exothermic

decomposition for pure RDX, RDX+CuO, RDX+Fe_2O_3, RDX+CuO+Fe_2O_3, RDX+$CuFe_2O_4$-p and RDX+$CuFe_2O_4$-d are 241.3, 239.9, 236.9, 237.7, 220.0 and 231.4 ℃, respectively. Here, the effects of CuO, Fe_2O_3, and CuO+Fe_2O_3 are unconspicuous, but $CuFe_2O_4$-p and $CuFe_2O_4$-d significantly influence the decomposition of RDX. The peak shapes of RDX+$CuFe_2O_4$-p and RDX+$CuFe_2O_4$-d were also significantly different from those of other four curves. These results should be ascribed two major reasons: (1) the positive synergistic effect between Cu and Fe in $CuFe_2O_4$ nanoparticles led to higher catalytic activity than CuO and Fe_2O_3; (2)the hollow structure of $CuFe_2O_4$ increased its specific surface areas and improved the diffusion rate of the decomposed molecules. Furthermore, the decomposition heats of pure RDX, RDX+$CuFe_2O_4$-p and RDX+$CuFe_2O_4$-d are calculated to be about 776, 970, and 872 J g^{-1} respectively, indicating that $CuFe_2O_4$-p and $CuFe_2O_4$-d not only accelerated the thermal decomposition of RDX, but also increased the decomposition depth, which would be favourable to improve the burning rate of solid propellant. Obviously, $CuFe_2O_4$-p has superior catalytic performance compared to $CuFe_2O_4$-d because of its smaller particle size and larger specific surface area, which is consistent with the SEM and BET results.

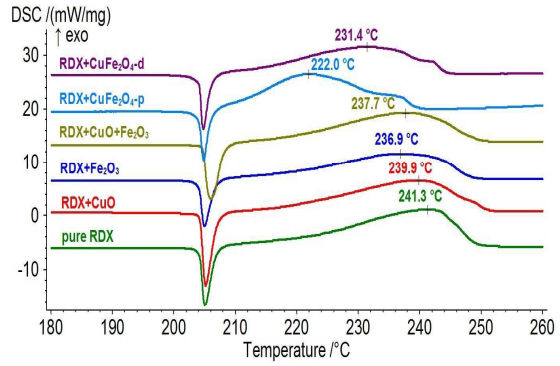

Fig. 5. DSC curves for pure RDX and RDX mixed with different samples

3.3 Influence on thermal decomposition of FOX-7

DSC results (**Fig. 6**) suggests that the first peak temperatures of exothermic decomposition for FOX-7+CuO, FOX-7+Fe_2O_3, FOX-7+CuO+Fe_2O_3, FOX-7+$CuFe_2O_4$-p and FOX-7+$CuFe_2O_4$-d are 219.9, 221.0, 219.9, 219.9 and 218.5 ºC respectively, which are all less than that of pure FOX-7 (234.6 ºC) by

approximately 15 ºC. However, the apparent decomposition heats for the above mixtures are 620, 632, 528, 643 and 679 J g^{-1} respectively, which are much larger than that of pure FOX-7 (489 J g^{-1}). FOX-7+$CuFe_2O_4$-p and FOX-7+$CuFe_2O_4$-d released more heat than others. **Fig. 6** shows that the second peak temperatures for FOX-7+Fe_2O_3, FOX-7+CuO+Fe_2O_3, FOX-7+$CuFe_2O_4$-p, and FOX-7+$CuFe_2O_4$-d are less than that of pure FOX-7 (294.9 ºC) by 6.6, 4.2, 12.2, and 9.1 ºC, respectively. However, this temperature is even higher with the addition of CuO. Therefore, $CuFe_2O_4$-p and $CuFe_2O_4$-d play better catalytic role than others on the thermal decomposition of FOX-7. The catalytic activity of $CuFe_2O_4$-p is still stronger than $CuFe_2O_4$-d on FOX-7 thermal decomposition. Between the two energetic materials, $CuFe_2O_4$-p and $CuFe_2O_4$-d show higher catalytic decomposition activity on RDX than on FOX-7.

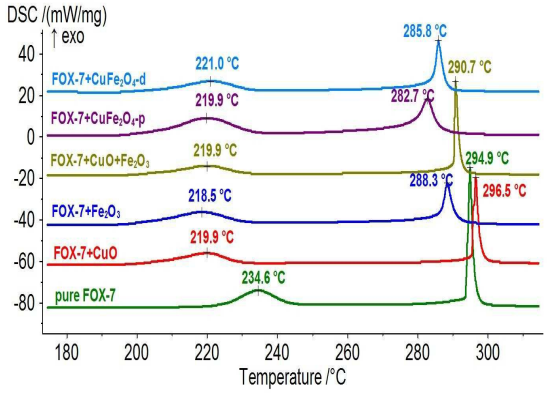

Fig. 6. DSC curves of pure FOX-7 and FOX-7 mixed with different samples

3.4 Apparent activation energy

The apparent activation energy (E_a) of the decomposition process was evaluated by Kissinger method with DSC data from different heating rates (5.0, 10.0, 15.0, and 20.0 °C min^{-1}). The E_a values for four mixtures were obtained and listed in Table 2. We can see that the E_a values of the decomposition process for RDX+$CuFe_2O_4$-p and RDX+$CuFe_2O_4$-d are less than the literature value of pure RDX (172.6 kJ mol^{-1}) [36] by 37.7 and 28.4 kJ mol^{-1}, respectively. The E_a values of the decompoition process for FOX-7+$CuFe_2O_4$-p and FOX-7+$CuFe_2O_4$-d are less than the literature value of pure FOX-7 (249.9 kJ mol^{-1}) [37] by 40.1 and 30.5 kJ mol^{-1}, respectively. The reduction in

the apparent activation energy is greater with $CuFe_2O_4$-p than with $CuFe_2O_4$-d, which is also ascribed to its smaller particle size and larger specific surface area. These results indicate that $CuFe_2O_4$-p and $CuFe_2O_4$-d can reduce the apparent activation energy of the decomposition process, increase the decomposition rate and show good catalytic decomposition activity.

Table 2 Apparent activation energies of the decomposition process for different samples

Sample	E_a (kJ mol^{-1})	r
RDX	172.6	0.982
RDX+$CuFe_2O_4$-p	134.9	0.998
RDX+$CuFe_2O_4$-d	144.2	0.991
FOX-7	249.9	0.995
FOX-7+$CuFe_2O_4$-p	209.8	0.984
FOX-7+$CuFe_2O_4$-d	219.4	0.997

4. Conclusion

In summary, hollow $CuFe_2O_4$-p and $CuFe_2O_4$-d nanospheres were successfully prepared and were characterized by XRD, XPS, SEM, TEM, HRTEM, EDS and BET methods. $CuFe_2O_4$-p has samller size and higher BET specific surface area compared to $CuFe_2O_4$-d. DSC results indicate that $CuFe_2O_4$-p and $CuFe_2O_4$-d can greatly reduce the decomposition temperature, increase the decomposition heat, and show higher catalytic decomposition activity on RDX and FOX-7 compared to CuO, Fe_2O_3 and CuO+Fe_2O_3. The E_a values of the decomposition process with the catalytic action of $CuFe_2O_4$-p and $CuFe_2O_4$-d decrease by 37.7 and 28.4 kJ mol^{-1} for RDX, 40.1 and 30.5 kJ mol^{-1} for FOX-7, respectively. The reason for the good catalytic decomposition activity of $CuFe_2O_4$ should be the active chemical nature and hollow structure. The catalytic performance of $CuFe_2O_4$-p is superior to that of $CuFe_2O_4$-d because of its smaller particle size and larger specific surface area.

Acknowledgments

This investigation received financial assistance from the National Natural Science Foundation of China (21241003), Postdoctoral Science Foundation of China

(2014M552480) and Postdoctoral Science Foundation of Shanxi Province.

References

[1] R. A. Isbell and M. Q. Brewster, *Prop. Explos. Pyrotech.*, 1998, **23**, 218-224.

[2] D. M. Badujar, M. B. Talawar, S. N. Asthana and P. P. Mahulikar, *J. Hazard. Mater.*, 2008, **151**, 289-305.

[3] A. A. Said and R. A. Qasmi, *Thermochim. Acta.*, 1996, **275**, 83-91.

[4] D.V. Survase, M. Gupta and S. N. Asthana, *Prog. Cryst. Growth. Ch.*, 2002, **45**, 161-165.

[5] W. F. Chen, F. S. Li, J. X. Liu, H. C. Song and J. Y. Yu, *Chin. J. Catal.*, 2005, **26**, 1073-1077.

[6] Y. P. Tong, Y. P. Wang, Z. X. Yu, X. Wang, X. J. Yang and L. D. Lu, *Mater. Lett.*, 2008, **62**, 889-891.

[7] K. Faungnawakij, R. Kikuchi, T. Fukunaga and K. Eguchi, *Appl. Catal. A-Gen.*, 2007, **333**, 114-121.

[8] Z. Z. Pei and Y. Zhang, *Mater. Lett.*, 2008, **62**, 504-506.

[9] T. X. Liu, B. X. Li, Y. G. Hao and Z. Y. Yao, *Chem. Eng. J.*, 2014, **244**, 382-390.

[10] P. K. Seon, U. L. Dong and K. K. Eun, *Curr. Appl. Phys.*, 2010, **10**, S478-S480.

[11] P. Ujwol, K. Henning, N. Rodrigo, A. Sahar, J. Vladislav, M. Philipp, A. Hasan, S. Alberto, S. Helmut and K. Dietmar, *Nano Energy*, 2014, **6**, 167-172.

[12] E. Alizadeh-Gheshlaghi, B. Shaabani, A. Khodayari, Y. Azizian-Kalandaragh and R. Rahimi, *Powder Technol.*, 2012, **217**, 330-339.

[13] Y. Yuan, J. Wei, Y. J. Wang, P. Shen, F. S. Li, P. Y. Li, F. Q. Zhao and H. X. Gao, *Appl. Surf. Sci.*, 2014, **3039**, 354-359.

[14] N. N. Zhao, C. C. He, J. B. Liu, H. J. Gong, T. An, H. X. Xu, F. Q. Zhao, R. Z. Hu, H. X. Ma and J. Z. Zhang, *J. Solid State Chem.*, 2014, **219**, 67-73.

[15] X. D. Zheng, P. Li, S. L. Zheng and Y. Zhang, *Powder Technol.*, 2014, **268**, 446-451.

[16] I. P. S. Kapoor, P. Srivastava and G. *Singh, Prop. Explos. Pyrotech.*, 2009, **34**, 351-356.

[17] Y. F. Zhang, N. N. Wang, Y. T. Huang, W. B. Wu, C. Huang and C. G. Meng, *Ceram. Int.*, 2014, **40**, 11393-11398.

[18] W. J. Zhang, P. Li, H. B. Xu, R. D. Sun, P. H. Qing and Y. Zhang, *J. Hzarad. Mater.*, 2014, **268**, 273-280.

[19] L. L. Liu, F. S. Li, L. H. Tan, M. Li and Y. Yang, *Prop. Explos. Pyrotech.*, 2004, **29**, 34-38.

[20] Y. P. Wang, X. J. Yang, L. D. Lu and X. Wang, *Thermochim. Acta.*, 2006, **443**, 234-239.

[21] T. Liu, L. S. Wang, P. Yang and B. Y. Hu, *Mater. Lett.*, 2008, **62**, 4056-4058.

[22] G. Singh, I. P. S. Kapoor and S. Dubey, *J. Alloys. Compd.*, 2009, **480**, 270-274.

[23] Y. Sharma, N. Sharma, G. V. Subba Rao and B. V. R. Chowdari, *Adv. Funct. Mater.*, 2007, **17**, 2855-2861.

[24] R. Q. Wan, C. H. Jia and W. F. Zhang, *J. Alloy. Compd.*, 2012, **544**, 1-5.

[25] A. Singh, V. Singh, K. K. Bamzai, *Mater. Chem. Phys.*, 2015, **155**, 92-98.

[26] Y. M. Liu, Z. J. Li, H. Lv, H. B. Tang, X. Y. Xing, *Mater. Lett.*, 2013, **108**, 84-87.

[27] Z. T. Zhang, A. J. Rondinone, J. X. Ma, J. Shen and S. Dai, *Adv. Mater.*, 2005, **17**,1415-1419.

[28] W. Ponhan and S. Maensiri, *Solid State Sci.*, 2009, **11**, 479-484.

[29] Z. P. Sun, L. Liu, D. Z. Jia and W. Y. Pan, *Sensor Actuat B-chem.*, 2007, **125**, 144-148.

[30] L. Su, W. J. Qin, H. G. Zhang, Z. U. Rahman, C. L. Ren, S. D. Ma and X. G. Chen, *Biosens. Bioelectron.*, 2015, **63**, 384-391.

[31] L. Luo, R. R. Cui, H. Qiao, K. Chen, Y. Q. Fei, D. W. Li, Z. Y. Pang, K. Liu and Q. F. Wei, *Electrochim. Acta.*, 2014, **144**, 85-91.

[32] X. H. Wu, W. W. Wu, Y. N. Li, F. Li and S. Liao, *Mater. Lett.*, 2015, **138**, 192-195.

[33] Y. B. Ding, L. H. Zhu, N. Wang and H. Q. Tang, *Appl. Catal. B-Environ.*, 2013, **129**, 153-162.

[34] N. Shimoda, Muroyama H, Matsui T, Faungnawakij K, Kikuchi R and K. Eguchi, *Appl. Catal. A-Gen.*,

2011, **409-410**, 91-98.

[35] A. Kezzima, N. Nasrallaha, A. Abdi and M. Trari, *Energy Convers. Manage.*, 2011, **52**, 2800-2806.

[36] X. P. Fan, X. Wang, Z. R. Liu and H. M. Tan, *Energetic materials*, 2005, **13**, 284-287. (in Chinese)

[37] Q. B. Fu, Y. J. Shu, Y. G. Huang and J. H. Zhou, *Journal of Sichuan Ordnance*, 2009, **30**, 15-17. (in Chinese)